Journal of Applied Fluid Mechanics, Vol. 17, No. 10, pp. 2215-2227, 2024.
Available online at www.jafmonline.net, ISSN 1735-3572, EISSN 1735-3645.
https://doi.org/10.47176/jafm.17.10.2574

Numerical Study and Parameter Optimization of a Dual-jet Based Large Particle Collection System for Deep-sea Mining

Y. Z. Jin[1, 2†], Q. K. Yao[1], Z. C. Zhu[1, 2] and X. M. Zhang[1]

[1] *Zhejiang Key Laboratory of Multiflow and Fluid Machinery, Zhejiang Sci-Tech University, Hangzhou, Zhejiang, 310018, China*
[2] *Hefei General Machinery Research Institute Co., Ltd., Hefei, Anhui, 230061, China*

†*Corresponding Author Email: yzjin@zstu.edu.cn*

ABSTRACT

A dual-jet collecting device is highly efficient at picking up small-sized polymetallic nodules; however, its performance is not as effective for large nodules in deep-sea mining. To address this problem, numerical simulations have been conducted to thoroughly investigate the flow characteristics and particle motions during the collection of larger nodules. The collection performance of the enhanced device is analyzed across varying front jet velocities (V_f), suction pressures (P_{out}), and nozzle heights (h/d). The results reveal that increasing V_f improves the drag force and particle velocity in the jet impingement and upwelling zones, facilitating nodule lifting movement and transport. However, increasing P_{out} reduces the drag forces in these zones while increasing the particle velocity in the upwelling zone. A large P_{out} is not conducive to nodule initiation but has benefits for transport. Increasing h/d reduces the drag force in the anti-gravity direction in the jet impingement zone. The improved collecting device attains a pick-up efficiency that exceeds 80% for large-sized nodules when $h/d < 1.3$. The pick-up efficiency with suction pressure, which remains 40%, is higher than that without suction pressure when $h/d > 1.3$. The research findings may shed light on the design of more efficient dual-jet collection systems.

Article History

Received January 12, 2024
Revised April 9, 2024
Accepted May 2, 2024
Available online July 31, 2024

Keywords:

Deep-sea mining
Collecting device
Dual-jet
Hydraulic collection
Polymetallic nodules

1. INTRODUCTION

Owing to the continuous depletion of terrestrial mineral resources, countries around the world are gradually shifting their focus toward deep-sea mineral deposits, including polymetallic nodules, polymetallic sulfides, and cobalt-rich ferromanganese crusts (Liu et al., 2023). Polymetallic nodules, also called manganese nodules, contain abundant manganese (29%), iron (6%), silicon (5%), aluminum (3%), nickel (1.4%), cobalt (0.25%), and other elements, and this makes them the most abundantly known deep-sea mineral resources. Polymetallic nodules are thus, considered the most valuable for exploitation (Kim et al., 2024). Polymetallic nodules generally exhibit a spherical or elliptical shape with a smooth surface, ranging in diameter from 2 cm to 10 cm. They are primarily found in seabed sediments at depths ranging from 4000 meters to 6000 meters, often in a semi-buried state, with some nodules entirely concealed by sediment (Liu et al., 2024). Based on the results of offshore trials conducted by Ocean Management Incorporated in 1978, hydraulic collection methods have emerged as the mainstream method for nodule harvesting, offering higher efficiency than mechanical collection methods and superior adaptability to variations in seafloor topography (Guo et al., 2023). Three distinct hydraulic collection methods have been employed in offshore experiments, encompassing the suck-up-based method, the Coandă effect-based method, and the dual-jet method. In the suck-up-based method, nodules are directly drawn into the pipeline through suction action. The Coandă effect-based method involves the generation of pressure differentials by high-speed wall jets, which increase the uplift of the nodules. Within the dual-jet method, nodules are first lifted from the seabed through the combined influence of front and rear jets, whereupon they are carried upward by the upwelling flow.

Numerous investigators have conducted extensive research on these three hydraulic collection methods. In their research on the suck-up-based method, Zhao et al. (2018) conducted experimental research on the collection mechanisms of spherical particles. Under conditions where the maximum tolerance was less than 15%, the researchers derived empirical formulas for vertical forces and criteria for vertical particle initiation. The characteristics

NOMENCLATURE			
V_f	front jet velocity	F_{dx}	particle drag force in the x-direction
V_r	rear jet velocity	F_{dz}	particle drag force in the z-direction
P_{out}	pressure at the nodule outlet	V	particle velocity
d	particle diameter	V_z	particle velocity in the z-direction
h	nozzle height	V_s	particle slip velocity
V_t	towing velocity	X	x-direction position
F_d	particle drag force	Z	z-direction position

of the suction flow field were first ascertained through flow visualization experiments and then used to elucidate the force interactions of particles within the suction flow field. Chen et al. (2020) employed the computational fluid dynamics-discrete element method (CFD–DEM) to investigate the particle collection process under various initial motion conditions. They concluded that the additional lift on spheres was provided by the coupling of vortices around the spheres with the main stream. Zhang et al. (2021) conducted experiments to examine the critical suction velocity necessary to elevate coarse particles. Insight into the characteristics of solid-liquid two-phase flow was obtained, and a fitting formula for the critical suction velocity was proposed. Zhao et al. (2021b) introduced a hydraulic ore-collecting device based on the principle of spiral flow. Notably, this device was found to possess advantages in increasing suction and critical bottom clearance, thereby minimizing operational flow rates. Xia et al. (2023) employed the CFD-DEM method to simulate the hydraulic suction process of ore particles. The effects of different suction velocities on the lateral displacement offset, drag coefficient and Reynolds number of particles were studied on the basis of the analysis of the flow field characteristics. It was determined that the lift force was caused by the different flow velocities of the upper and lower flow fields. At the same time, the empirical equation of vertical force was proposed.

In the research of the Coandă effect-based method, Cho et al. (2019) conducted experiments to study the relationship between design variables such as the nozzle width, baffle radius, water jet flow rate, the distance between the nozzle and the ground, and the nodule pick-up efficiency. Zhao et al. (2021a) used particle image velocity (PIV) experimental methods and analyzed the similarities and differences in nodule collection between the suck-up-based method and the Coandă effect-based method. Particle motion was captured using the visual object tracking method from OpenCV, and it was observed that the Coandă effect-based method required a smaller flow rate. Yue et al. (2021a) obtained velocity distributions for the suck-up-based method and the Coandă effect-based method through PIV experiments and numerical methods. They validated the numerical method based on the realizable k-ε model for predicting the collection flow field. Jia et al. (2023) simplified the modeling of jet flows over logarithmic spiral surfaces to investigate the flow characteristics and lift capability of a newly designed Coandă effect-based collector. It was found that the lift capability was stronger with a higher jet exit velocity, local curvature, or a nondimensional jet slot height. The growth rate representing the width of the main jet flow increased proportionally with the downstream distance.

Compared to the two methods mentioned above, the dual-jet method has the following advantages: a large collection range, high pick-up efficiency, low flow consumption, direct jet action on nodules, and ease of collecting semi-buried or fully buried nodules. Yang and Tang (2003) carried out experimental research on dual-jet collecting devices and determined the conditions that ensured high pick-up efficiency by varying the jet flow rate, towing velocity, and baffle shape as experimental parameters. Hong et al. (1999) examined the influence of structural parameters on pick-up efficiency through experiments and provided the range of values for the main structural parameters when designing collecting devices. Yue et al. (2021b) performed a comparative study of three hydraulic collection methods using numerical methods. They compared the advantages and disadvantages of different methods in terms of pick-up efficiency and seabed flow disturbance. They determined that the dual-jet method required the lowest flow rate when the pick-up efficiency reached 80% for all methods. Su et al. (2023) compared two different induced flow type and suction type back-end action methods. The numerical simulation method was used to compare the collection efficiency, and an energy analysis and quantitative evaluation method was proposed. The researchers found that the energy utilization rate of the induced flow pattern was higher than that of the suction flow pattern. However, current research on the dual-jet method is mostly focused on small-sized nodules, resulting in low pick-up efficiency for large-sized particles. The particle–fluid coupling flow mechanism behind this phenomenon is not yet clear. Hence, it is significant to further investigate the motion characteristics of large-sized nodules inside the collection system.

The original dual-jet collecting device is improved in this study by optimizing its structure for the collection of large-sized nodules. The collection process is simulated in a seawater environment. The characteristics of the flow field and particle motion are analyzed at various front jet velocities, suction pressures, and nozzle heights to the ground The research findings discussed in this paper can guide the design and optimization of dual-jet collection systems.

2. COLLECTING DEVICE MODEL

In the present study, a model of a dual-jet collecting device is redesigned, with the basis being a prototype collecting device developed by KRISO (Hong et al., 1999). To enhance the realism of the simulation, the collecting device is integrated with a water environment,

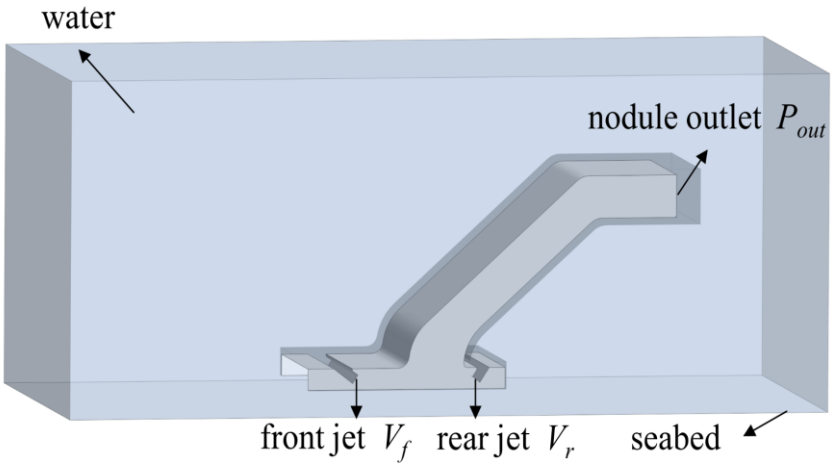

(a) 3D view

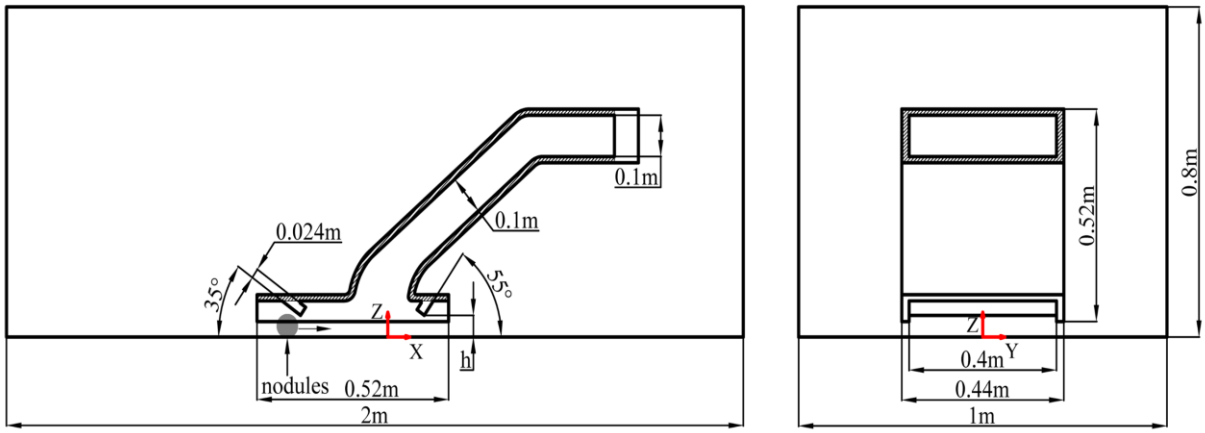

(b) 2D view

Fig. 1 Geometry model of dual-jet

as depicted in Fig. 1(a).

The model's dimensions are redesigned. The collecting device has an inner width of 0.4 m and an overall height of 0.52 m. The angle between the front jet and the ground is 35°, whereas the angle between the rear jet and the ground is 55°. With the primary focus on the collection of large particles (50 mm), the widths of both the front and rear jets are increased to 0.024 m. To achieve a more rapid and uniform distribution of water jets in the y-direction and obtain a uniform velocity state, a simplification is made to the jet inlets by using a rectangular cross section. The coordinate origin ($X = Y = Z = 0$) is located directly below the collecting device. More detailed model parameters are presented in Fig. 1(b). Multiphase interactions between seawater, nodules, and sediments characterize the actual mining operation. To reduce the computational load and simplify the physical aspects of hydraulic collection, this study makes the following assumptions. Nodules are assumed to be spherical with a smooth surface. Only the interactions between nodules and seawater are considered, while the influence of seabed sediments on particle collection is ignored. Nodules are transported at a velocity of V_t by the injectors.

In compliance with the Froude similarity criterion, this study simulates the primary parameters as shown in Table 1 (Yue et al., 2021b). The front jet velocity V_f, the rear jet velocity V_r and the suction pressure P_{out} are obtained based on the China sea test data and multiple simulation trials. The ratio of V_f to V_r is 4:3. The jet height to the ground h needs to be slightly larger than the diameter of nodule d. The pick-up efficiency η is defined as the ratio of the weight of nodules exiting the nodule outlet to the total weight of nodules. During the initial

Table 1 Main parameters

	Main parameters	Value
V_f	Front jet velocity/(m·s^{-1})	3−5
V_r	Rear jet velocity/(m·s^{-1})	2.25−3.75
P_{out}	Suction pressure/(Pa)	0 to −2000
h	Jet height to the ground/(mm)	52.5−75
ρ	Density of water/(kg·m^{-3})	1030
ρ_p	Density of nodules/(kg·m^{-3})	2100
d	Diameter of nodules/(mm)	50
μ	Dynamic viscosity of water/(Pa·s)	0.0011
V_t	Towing velocity/(m·s^{-1})	0.8
η	Pick-up efficiency	

stage, nodules are uniformly distributed along a line (X = −0.5 m), with a spacing of 0.12 m in the y-direction. Subsequently, the nodules are transported into the collecting device at a velocity of V_t = 0.8 m/s.

3. NUMERICAL METHOD

In this study, STAR-CCM + 16.02 is selected as the computational fluid dynamics (CFD) code to simulate the process of hydraulic collection. The Eulerian–Lagrangian model is used to calculate the multiphase flow. Because of the excellent performance of the realizable k-epsilon two-layer model in solving complex flow problems with high Reynolds numbers, this model is selected for the turbulence model. Furthermore, the discrete element method (DEM) model is used to simulate the dynamic characteristics of the particles.

3.1 Governing Equations

The continuity equation of a fluid describes the continuity characteristics of a fluid in space, and the momentum conservation equation of a fluid describes the conservation law of momentum in the process of fluid motion. The Navier–Stokes equations of incompressible flow are expressed as follows:

$$\nabla \cdot \left(\rho_f \boldsymbol{v} \right) = 0 \tag{1}$$

$$\frac{\partial \left(\rho_f \boldsymbol{v} \right)}{\partial t} + \nabla \cdot \left(\rho_f \boldsymbol{v} \otimes \boldsymbol{v} \right) = -\nabla \cdot \left(p\boldsymbol{I} \right) + \nabla \cdot \boldsymbol{T} + \boldsymbol{f}_b \tag{2}$$

where, ∇ is the divergence operator, ρ_f is the density of the fluid, $\boldsymbol{v}$ is the velocity vector of the fluid, t is the time, p is the pressure, $\boldsymbol{I}$ is the unit tensor, $\boldsymbol{T}$ is the viscous stress tensor and $\boldsymbol{f}_b$ is the resultant force of various volume forces acting on the unit volume of the continuum.

The Reynolds number Re is a dimensionless number used to characterize the flow of a fluid. Its equation is expressed as follows:

$$\mathrm{Re} = \frac{\rho_f v L}{\mu} \tag{3}$$

where v is the velocity of the fluid, L is the characteristic length, and μ is the dynamic viscosity of the fluid. In this study, we define v as the front jet velocity and L as the width of the front jet. The Reynolds number range is between 65000 and 120000.

3.2 Turbulence Model

In the physical model, the collecting device and the seabed can be considered complex geometric solid walls, with an internal flow characterized by high Reynolds number turbulent flow. The realizable k-epsilon two-layer model (RKE 2L) is employed, combining the realizable k-epsilon model with a two-layer model. When simulating high-Reynolds-number flows, vortex structures are effectively described by this model, providing more accurate predictions of turbulent characteristics within the boundary layer near solid walls (Shih et al., 1995). The transport equations of the turbulent kinetic energy k and turbulent dissipation rate ε are shown as follows:

$$\frac{\partial}{\partial t}\left(\rho_f k \right) + \nabla \cdot \left(\rho_f k \bar{\boldsymbol{v}} \right) = \nabla \cdot \left[\left(\mu + \frac{\mu_t}{\sigma_k} \right) \nabla k \right] + P_k - \rho\left(\varepsilon - \varepsilon_0 \right) + S_k \tag{4}$$

$$\frac{\partial}{\partial t}\left(\rho_f \varepsilon \right) + \nabla \cdot \left(\rho_f \varepsilon \bar{\boldsymbol{v}} \right) = \nabla \cdot \left[\left(\mu + \frac{\mu_t}{\sigma_\varepsilon} \right) \nabla \varepsilon \right] + \frac{1}{T_e} C_{\varepsilon 1} P_\varepsilon - C_{\varepsilon 2} f_2 \rho_f \left(\frac{\varepsilon}{T_e} - \frac{\varepsilon_0}{T_0} \right) + S_\varepsilon \tag{5}$$

where, μ is the hydrodynamic viscosity, σ_k = 1, σ_ε = 1.2, $C_{\varepsilon 1}$ = max [0.43, γ/ (5 + γ)], $\gamma = S_k/\varepsilon$, $C_{\varepsilon 2}$ = 1.9, $f_2 = k/ [k + (v\varepsilon)^{1/2}]$, $T_e = k/\varepsilon$ is the large eddy time scale, P_k and P_ε are the results of the k-epsilon model, S_k and S_ε are the source terms specified by the user.

The turbulent viscosity μ_t is:

$$\mu_t = \lambda \mu_{t(k-\varepsilon)} + \left(1 - \lambda\right) \mu \left(\frac{\mu_t}{\mu} \right)_{2layer} \tag{6}$$

where, $\mu_{t(k\text{-}\varepsilon)} = \rho C_\mu f_\mu k T_e$, C_μ = 0.09, f_μ is the damping coefficient, λ is related to Re, and $(\mu_t/\mu)_{2layer}$ is calculated depending on the model variant.

3.3 DEM Model

A DEM model is a widely used approach to solving particle dynamics, treating particles as discrete entities with defined mass and shape and accounting for interaction forces between them. In numerical simulations, nodules are considered discrete-phase particles, and the coupling of CFD and DEM can be used to accurately depict particle behavior within a fluid. The conservation equation of momentum for a particle is expressed as follows:

$$m_p \frac{d\boldsymbol{v}_p}{dt} = m_p g + \boldsymbol{F}_{fp} + \boldsymbol{F}_{bp} \tag{7}$$

where, m_p is the particle mass, $\boldsymbol{v}_p$ is the instantaneous particle velocity, $\boldsymbol{F}_{fp}$ represents the forces that act on the surface of the particle, $\boldsymbol{F}_{bp}$ represents the body forces.

Particle–fluid interaction is primarily represented by $\boldsymbol{F}_{fp}$ in Eq. (7), which can be decomposed into:

$$\boldsymbol{F}_{fp} = \boldsymbol{F}_d + \boldsymbol{F}_f + \boldsymbol{F}_L + \boldsymbol{F}_p + \boldsymbol{F}_{vm} \tag{8}$$

where $\boldsymbol{F}_d$ is the drag force, $\boldsymbol{F}_f$ is the buoyant force, $\boldsymbol{F}_L$ is the lift force, $\boldsymbol{F}_p$ is the pressure gradient force, and $\boldsymbol{F}_{vm}$ is the virtual mass force.

Interactions between particles are simplified using a spring–damper model in the DEM model. The spring generates a repulsive force to push particles apart, while the damper generates viscous damping, allowing for collision types other than fully elastic collisions. The contact model utilized in this study is the Hertz–Mindlin nonslip contact model, where the contact forces between particles are described by:

$$\boldsymbol{F}_{bp} = \boldsymbol{F}_n + \boldsymbol{F}_t \tag{9}$$

where $\boldsymbol{F}_n$ is the normal force component and $\boldsymbol{F}_t$ is the tangential force component.

Furthermore, DEM particles have orientations and the equations of motion therefore incorporate the angular momentum conservation equations:

$$\boldsymbol{I}_p \frac{d\boldsymbol{\omega}_p}{dt} = \boldsymbol{M}_{fb} + \boldsymbol{M}_{pc} \tag{10}$$

where $\boldsymbol{I}_p$ is the particle moment of inertia, ω_p is the particle angular velocity, $\boldsymbol{M}_{fb}$ is the moment that acts on the particle, and $\boldsymbol{M}_{pc}$ is the moment that acts on an individual particle due to contact force.

3.3 Coupling Scheme of CFD–DEM

In this study, we consider the interactions between the dispersed phase and the continuous phase to be two-way coupling. The coupling indicates the way in which the momentum, heat, and mass are exchanged between the phases. The displacement of the continuous phase by the dispersed phase is considered through the volume fraction. The volume fraction of a Lagrangian phase represents the fraction of the local cell volume occupied by that phase. The particle governing equations yield the momentum change for each particle between the inlet and outlet, and the sum of all the momentum changes across the volumes provides the total momentum exchange with the fluid.

In the context of two-way coupling simulations, it is generally imperative that the size of the fluid grid size exceeds that of the particle. Considering the relatively substantial dimensions of the particles in this study, measures are taken to ensure the precision of the simulation outcomes. Particularly, the CFD is employed, incorporating the source smoothing method. When the particle dimensions exceed those of the grid, the grid cells surrounding the particles are amalgamated into larger composite cells. Afterward, the fluid velocity and pressure within each grid cell are computationally determined through a weighted averaging process. Additionally, the resultant fluid–particle interaction forces are distributed among the grid cells using the same weighting method. This approach helps maintain simulation accuracy in cases where particle dimensions exceed those of the grid cells.

In the CFD–DEM coupling approach, as illustrated in Fig. 2, particles are generated at predetermined time intervals, even as the DEM provides particle position and velocity data. The fluid flow field and fluid forces acting upon the particles are then determined by CFD using this data. Subsequently, the fluid forces are transmitted back to the DEM, providing particle motion data for the subsequent time step.

3.4 Boundary Conditions and Simulation Cases

With respect to boundary conditions, the front and rear jet surfaces are set as velocity inlets, while the nodule outlet is set as a pressure outlet. The internal and external surfaces of the collecting device, as well as the seabed, are set as nonslip walls. To alleviate the influence of seawater domain boundaries on simulation results, the top and the surroundings of the seawater domain are set as pressure

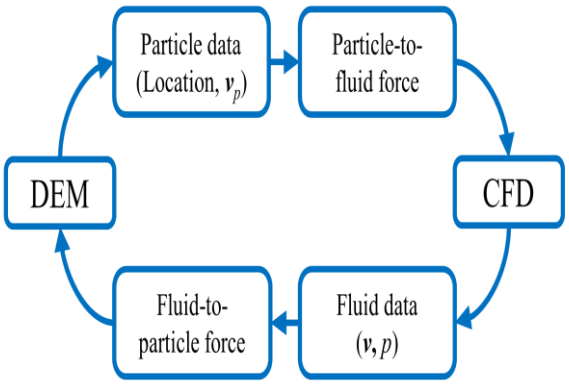

Fig. 2 CFD–DEM coupling process

Table 2 Simulation cases

	h/d	V_f/(m·s^{-1})	P_{out}/(Pa)
Case 1	1.05	3, 4, 5	0
Case 2	1.05	4	0, –1000, –2000
Case 3	1.05, 1.10, 1.15, 1.20, 1.25, 1.30, 1.35, 1.40, 1.45, 1.50	3, 4, 5	0, –1000, –2000

outlets. Table 2 delineates the test cases established in this study.

3.5 Mesh Generation and Convergence Analysis

The generated mesh is shown in Fig. 3(a). The meshes are refined near the collecting device to capture the velocity and pressure gradient in these regions. Mesh refinement is also specifically applied to the front and rear jets. The minimum mesh size is 2 mm, with a minimum mesh size-to-particle diameter ratio of 1:25.

To soften the impact of the mesh number and time step on the simulation results, a convergence analysis is performed to determine the optimal mesh resolution and time step. The average velocity of a monitoring point D_1 (X = Y = 0, Z = 0.1 m) is tracked and presented. Furthermore, the average velocity of particles in the average particle velocity zone is monitored, as depicted in Fig. 3(b). With grid refinement, the average velocity at D_1 and the average particle velocity increase, as shown in Fig. 4(a). When the mesh number reaches 1102194, the differences in the average velocity at D_1 for adjacent cases are 0.045% and 0.03%, and the differences in the particle average velocity are 0.353% and 0.09%, respectively. Consequently, convergence is considered to be achieved at a mesh number of 1102194.

With a decrease in the time step, there is a corresponding increase in the average velocity at D_1 and the average particle velocity, as shown in Fig. 4(b). When the time step size decreases to 0.01 s, the differences in the average velocity at D_1 for adjacent cases are 0.033% and 0.034%, and the differences in the particle average

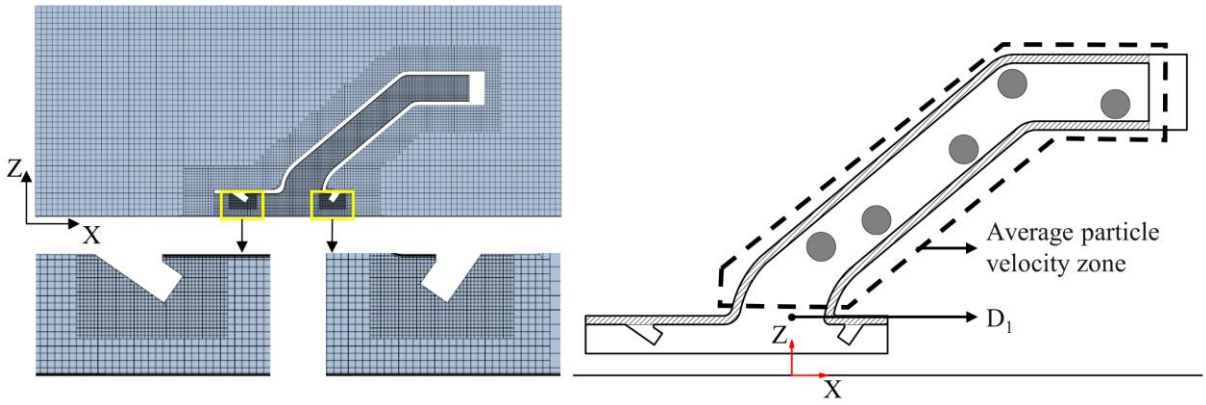

Fig. 3 Cross section mesh and monitoring settings

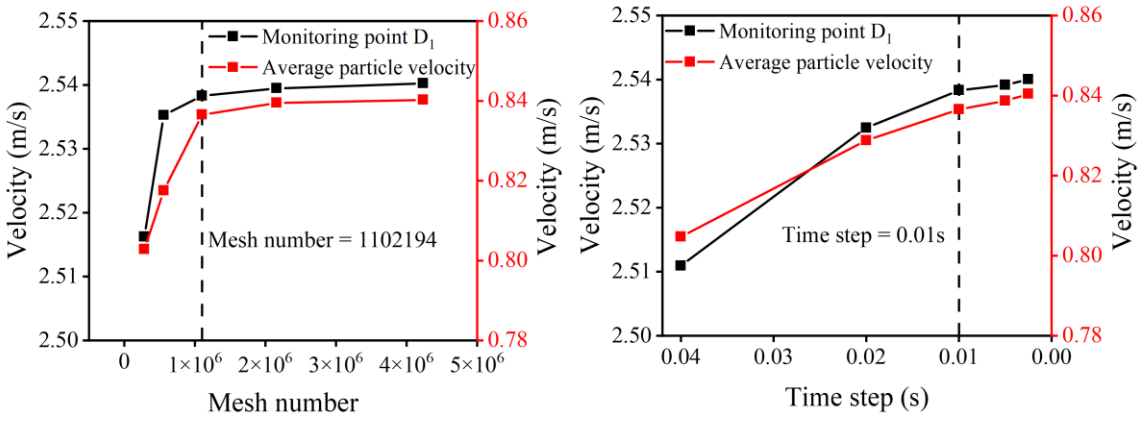

(a) Verification of mesh number independence (b) Verification of time step independence

Fig. 4 Convergence test

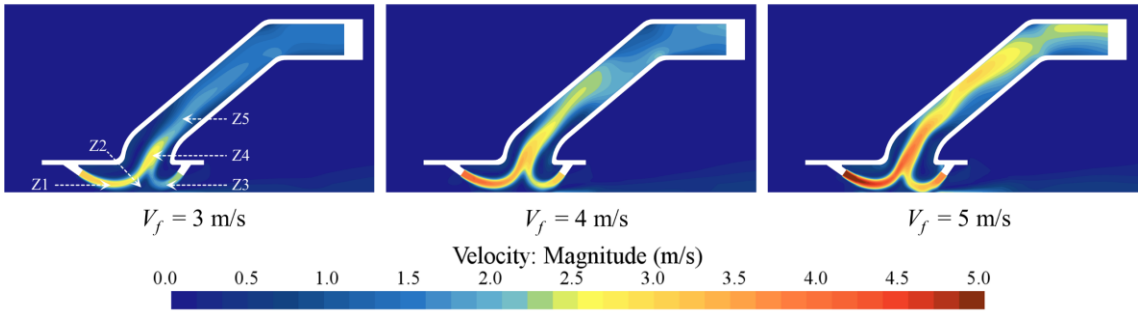

Fig. 5 Velocity distribution on the x-z plane (P_{out} = 0 Pa, h/d = 1.05)

velocity are 0.257% and 0.203%, respectively. Hence, convergence is considered to be achieved at a time step of 0.01 s. Based on the aforementioned analysis results, a mesh number of 1102194 and a time step of 0.01 s are selected for subsequent simulations.

4. RESULTS AND DISCUSSION

4.1 Influence of Front Jet Velocity V_f

The simulation results reveal that with a constant velocity ratio between the front and rear jets, variations in the nozzle heights h/d do not significantly affect the structure of the flow field. Therefore, the analysis in this section is based on the case where h/d = 1.05. The velocity contours at various front jet velocities V_f when P_{out} = 0 Pa are shown in Fig. 5. The flow field structure closely resembles the dual-jet collecting device designed by (Yue et al., 2021b). This structure can be broadly categorized into the following zones: the front jet impingement zone (Z1), confluence zone (Z2), rear jet impingement zone (Z3), upwelling zone (Z4), and transport zone (Z5). In Z1 and Z3, water jets, remaining almost uninfluenced by the seabed, are directed downward from the nozzles at an angled, resulting in a uniform flow velocity distribution. After the front and rear jets meet in Z2, the flow velocity rapidly decreases and the direction of the jet changes. The upwelling stream is formed by most of the jet water, flowing into the collecting device, whereas a small portion of the jet water spreads outward, parallel to the seabed.

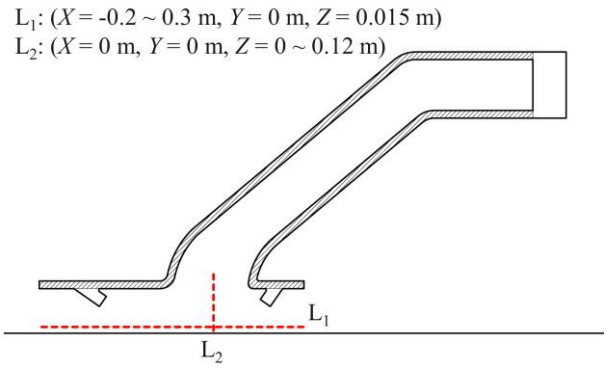

Fig. 6 Monitoring lines L_1 and L_2 on the x-z plane

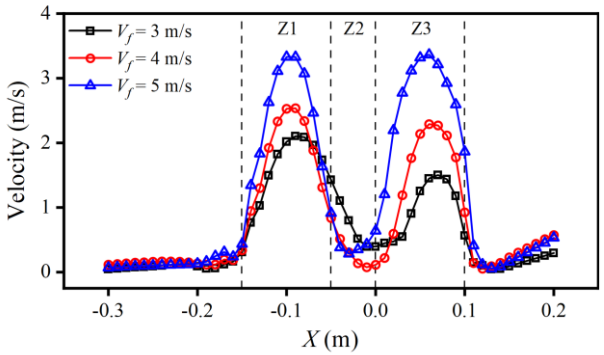

Fig. 7 Velocity distribution along monitoring line L_1

As depicted in Fig. 6, two monitoring lines, namely L_1 and L_2, are established to enhance the analysis of the flow field distribution within the collecting device. The velocity distribution along monitoring line L_1 is presented in Fig. 7. In Z1 and Z3, the velocity increases with a rise in V_f, signifying that the higher energy provided by the water jets can more effectively dislodge nodules embedded in the seabed sediment. In Z2, the velocity is relatively small because the two jet streams collide and change direction, creating a stagnation zone. Notably, the collecting device model maintains low flow velocities outside the above three zones, ensuring that the wall jet does not impact the nodules outside the collecting device. This design choice enhances pick-up efficiency and reduces disturbance to the seabed.

Pressure contours at various front jet velocities V_f are shown in Fig. 8, where the creation of a high-pressure zone in the confluence zone and a low-pressure zone above the jets can be observed. The pressure gradient between the upper and lower zones is conducive to particle lifting. The pressure distribution along monitoring line L_2, as shown in Fig. 9, is recorded. The pressure distribution remains similar for the various V_f. The pressure reaches its maximum value at Z = 0.035 m and gradually decreases, reaching its minimum value at Z = 0.09 m. When Z > 0.09 m, the pressure starts to increase slowly and the change becomes less noticeable. When V_f increases by 1 m/s, the maximum pressure values increase by 62.25% and 86.26%, and the pressure gradients increase by 42.05% and 65.47%. Increasing V_f significantly enhances the pressure gradient at the center of the collecting device.

The fluid–particle coupled collection process at a front jet velocity V_f = 4 m/s is shown in Fig. 10. At T = 1.0 s particles are generated and move into the collecting device with V_t = 0.8 m/s. The internal flow field of the collecting device is stable. At T = 1.2 s, the particles that first enter the collecting device are affected by the front jet, which leads to a decrease in the flow velocity in the jet impingement zone and affecting the formation of the upwelling. At T = 1.4 s, more particles enter the jet impingement zone, further weakening the velocity in this zone. However, under the influence of the rear jet, the particles are lifted and move toward the center of the collecting device. When T = 1.6 s, the collection flow field begins to recover and the particles are further lifted.

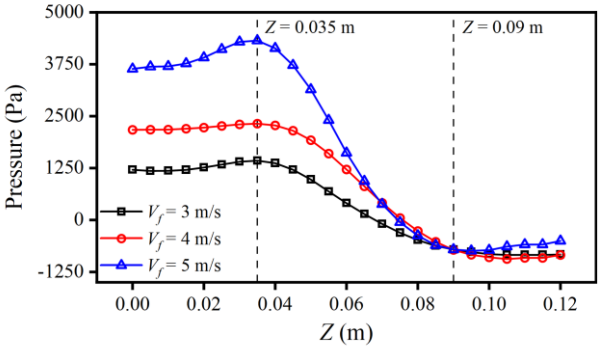

Fig. 9 Pressure distribution along monitoring line L_2

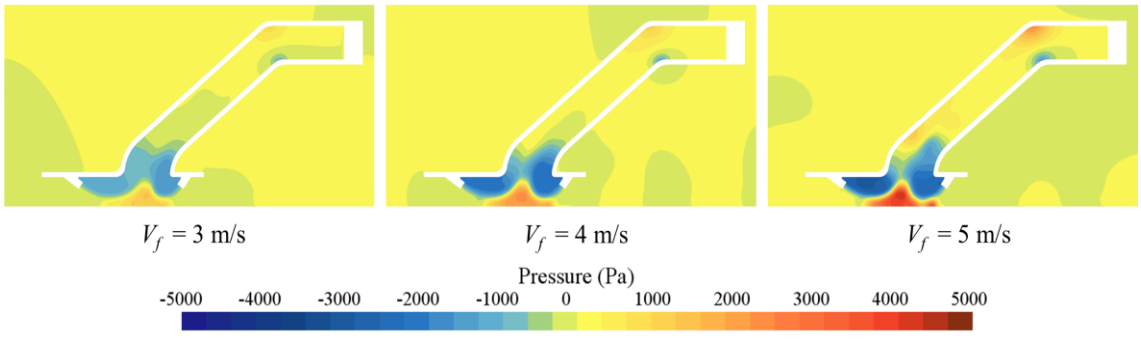

Fig. 8 Pressure distribution on the x-z plane (P_{out} = 0 Pa, h/d = 1.05)

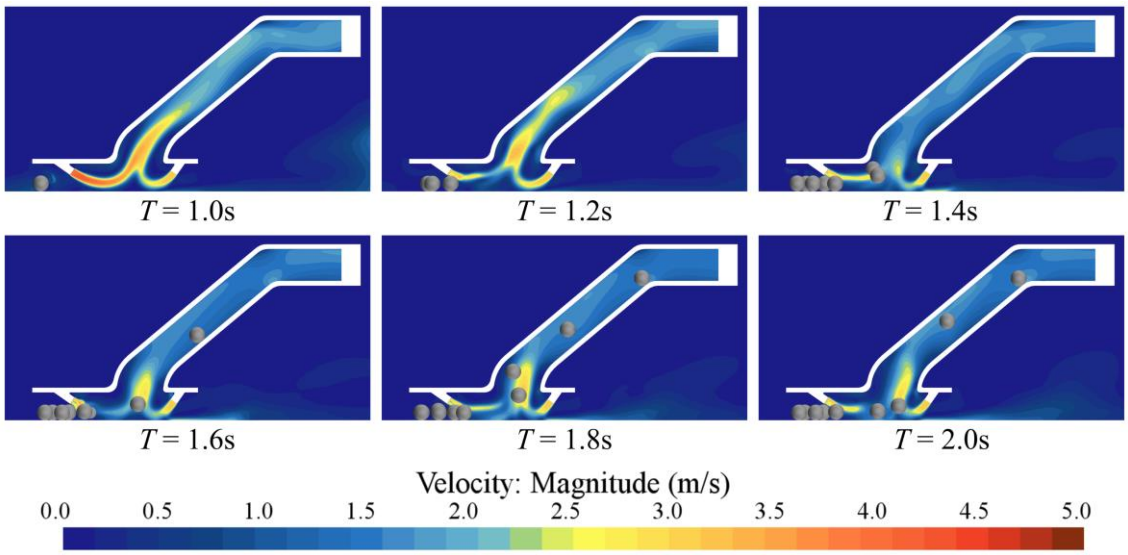

Fig. 10 Particle transport inside the collecting device (V_f = 4 m/s, P_{out} = 0 Pa, h/d = 1.05)

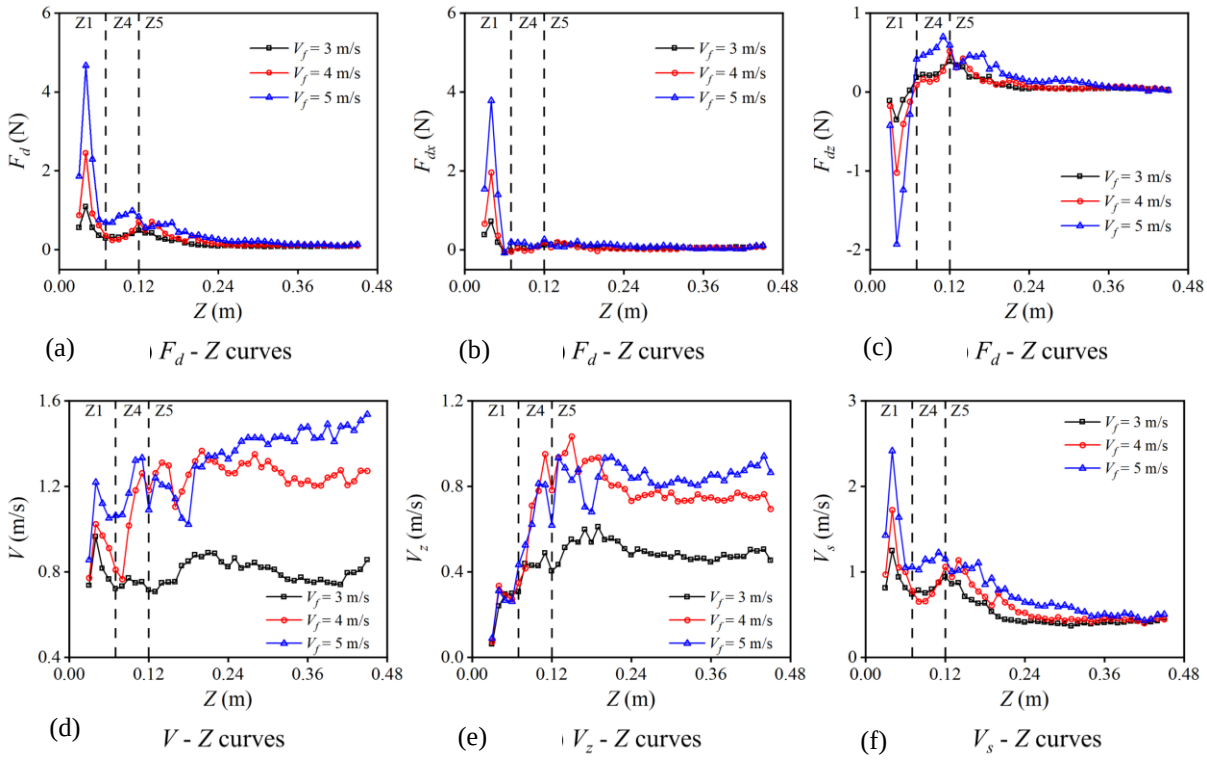

Fig. 11 Particle drag force and velocity distribution with three V_f (P_{out} = 0 Pa, h/d = 1.05)

Between T = 1.8 s and T = 2.0 s, the particles generated later also enter the collecting device and commence elevation. With an increase in height, the influence of the upwelling diminishes, causing particles to move along the rear wall of the collecting device.

The distributions of the average drag force F_d during the collection process at various front jet velocities V_f are illustrated in Fig. 11(a). Figure 10 shows that the particles mainly pass through three regions of the front jet impingement zone (Z1), upwelling zone (Z4), and transport zone (Z5). The peak of F_d is observed in Z1 at Z = 0.04 m, and then rapidly decreases. This phenomenon is attributed to the particles experiencing the impact of the front jet in this zone. When V_f increases by 1 m/s, the maximum F_d rises by 124.83% and 90.39%. In Z4, a slight increasing trend in F_d is noted, stemming from the uplift effect of the upwelling on particles in this zone. Additionally, in Z5, F_d gradually decreases and approaches zero, as the influence of the upwelling weakens with increasing height. To further analyze the composition of the drag force F_d, we examine the variations with the height Z of the average drag force in the x-direction F_{dx} and the average drag force in the z-direction F_{dz}. F_{dx} exhibits the same trend as F_d in Z1, in Fig. 11(b), indicating that the particles experience a force

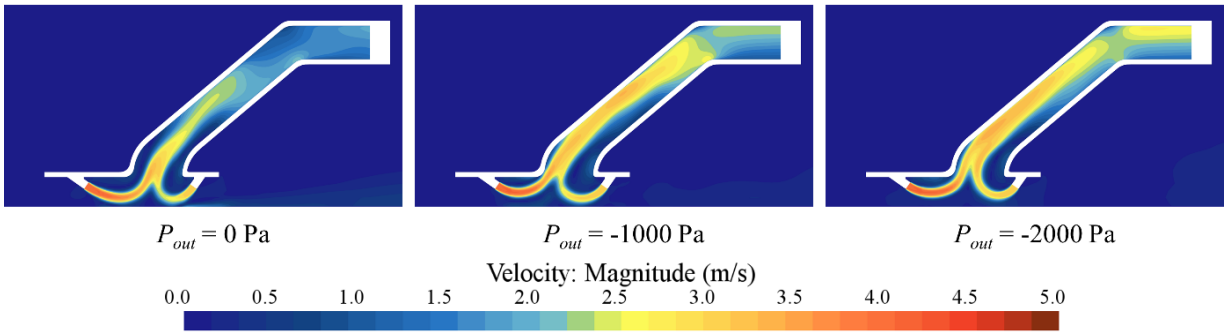

Fig. 12 Velocity distribution on x-z plane (V_f = 4 m/s, h/d = 1.05)

directed toward the interior of the collecting device in this zone. When V_f increases by 1 m/s, F_{dx} increases by 174.77% and 93%. In Z4 and Z5, F_{dx} fluctuates around zero, reflecting the weakening of the drag force in the x-direction under the influence of the upwelling. As shown in Fig. 11(c), F_{dz} initially decreases and then increases in Z1, even becoming negative, because the front jet is directed downward at an angle, exerting a downward force on the particles in the jet impingement zone. When V_f increases by 1 m/s, F_{dz} increases by 188.68% and 88.77%, indicating that the impact force of the jet strengthens with an increase in V_f. In Z4, an increasing trend is exhibited in F_{dz}, as the particles experience the uplifting effect of the upwelling, resulting in a positive value for F_{dz}. In Z5, as the influence of the upwelling weakens, F_{dz} decreases with an increase in Z. In summary, an increase in V_f not only increases both F_{dx} and F_{dz} in the jet impingement zone and hence facilitates their detachment from the seabed, but also enhances F_{dz} in the upwelling zone, favoring particle transport.

The distributions of the average particle velocity V during the collection process at various front jet velocities V_f are illustrated in Fig. 11(d). In Z1, V increases transiently and then decreases, which is caused by the impact of the front jet. In Z4, particles experience the influence of the upwelling, which results in an increasing trend in V as they accelerate upward. In Z5, particles move toward the outlet and the velocity shows fluctuations, likely arising from particle–wall collisions or particle-particle interactions. When V_f increases by 1 m/s, the average V in Z5 increases by 47.53% and 15.63%, which is beneficial for particle transport. Based on the primary direction of particle motion, the variations with the height Z of the average velocity in the z-direction V_z and the average slip velocity V_s are analyzed. As shown in Fig. 11(e), V_z continuously increases in both Z1 and Z4. When particles are located in Z5, V_z gradually stabilizes but still exhibits some fluctuations. V_z rises with the higher V_f in Z4 and Z5, but Z1 shows less sensitivity to V_f. In Fig. 11(f), V_s is relatively large in Z1 because the particles enter the collecting device with towing velocity V_t, significantly different from V_f. In Z4, as particles move upward under the influence of upwelling, there can be settling effects due to gravity, leading to an increase in V_s. In Z5, the particle motion gradually stabilizes, and the particle velocity approaches the fluid velocity, resulting in a gradual decrease in V_s with increasing Z. In summary, the upward

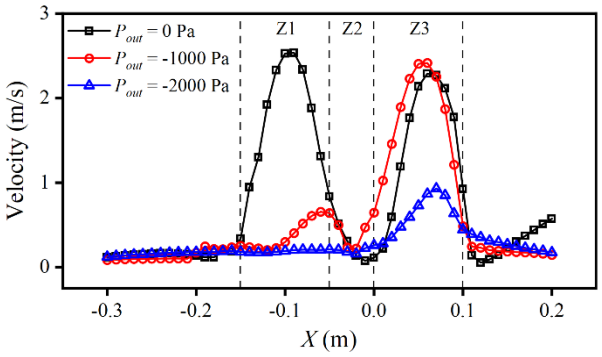

Fig. 13 Velocity distribution along monitoring line L_1

movement and transport of particles can be facilitated by increasing V_f.

4.2 Influence of Suction Pressure P_{out}

Velocity contours at three suction pressures P_{out} are shown in Fig. 12. When P_{out} = 0 Pa, both the front and rear jets exert their influence on the seabed. Nevertheless, at P_{out} = –1000 Pa, the front jet is elevated due to the wall attachment effect, resulting in upwelling along the upper side of the collecting device. At P_{out} = –2000 Pa, both the front and rear jets are elevated, leading to a diminished force on the seabed. Velocity distributions along monitoring line L_1 are similarly recorded, as shown in Fig. 13. With each increment of 1000 Pa in P_{out}, the maximum flow velocities in Z1 decrease by 287.14% and 219.74%. This indicates that as P_{out} increases, the impact of the jets on the seabed diminishes.

Pressure contours at various suction pressures P_{out} are shown in Fig. 14. When influenced by suction effects, the confluence zone noticeably shifts forward. The pressure distribution along monitoring line L_2, as shown in Fig. 15, is recorded. Notably, compared with P_{out} = 0 Pa, the near-surface pressure at the center position is ~0 Pa due to the forward movement of the convergence zone when the P_{out} is increased. When P_{out} = –1000 Pa, the change trend of the pressure at the center position with height is the same as that for P_{out} = 0 Pa, and the overall value decreases obviously. When P_{out} = –2000 Pa, the pressure increases slowly and then decreases slowly with the change of height and reaches the maximum at Z = 0.065 m. With each increase of 1000 Pa in P_{out}, the pressure gradient

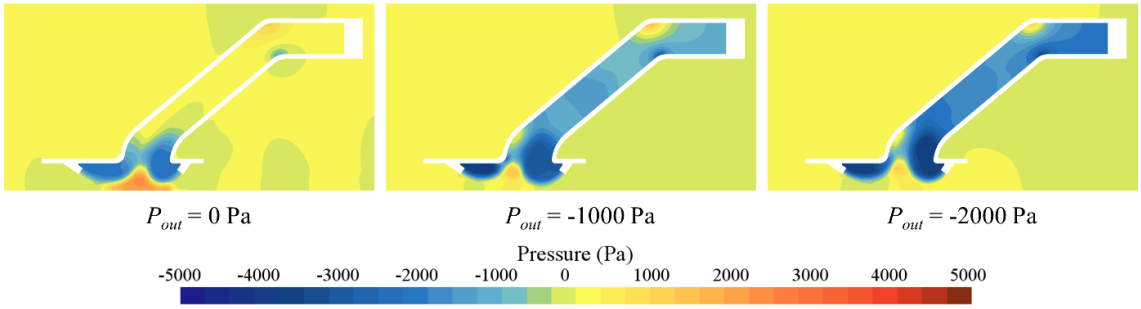

Fig. 14 Pressure distribution on x-z plane (V_f = 4 m/s, h/d = 1.05)

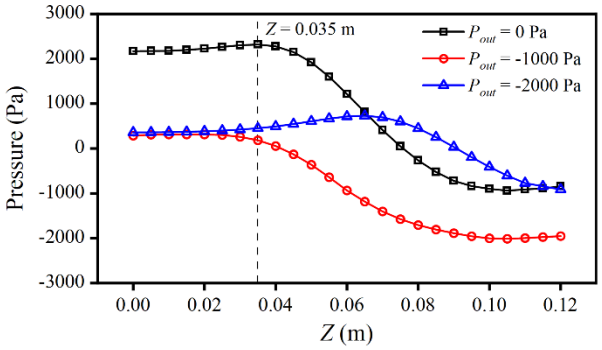

Fig. 15 Pressure distribution along monitoring line L_2

decreases by 29.01% and 29.22%. Increasing P_{out} leads to the forward shift of the confluence zone and reduces the pressure gradient at the center of the collecting device.

The distributions of the average drag force F_d during the collection process at various suction pressures P_{out} are illustrated in Fig. 16(a). The peak of F_d is observed in Z1 at Z = 0.04 m, followed by a rapid decrease, consistent with the distribution shown in Fig. 11(a). With every increment of 1000 Pa in P_{out}, the maximum F_d decreases by 5.78% and 54.29%. In Z4, under the conditions of suction pressure, F_d does not increase. Instead, it maintains a relatively low level. In Z5, F_d gradually decreases and approaches zero. The drag forces F_{dx} in the x-direction and F_{dz} in the z-direction with height Z are analyzed. In Fig. 16(b), F_{dx} exhibits a similar trend to F_d in Z1. With each increment of 1000 Pa in P_{out}, F_{dx} decreases by 20.96% and 46.4%. In Z4 and Z5, F_{dx} fluctuates near zero. In Fig. 16(c), F_{dz} in Z1 initially decreases and then increases and even becomes negative. With each increment of 1 m/s in V_f, the maximum F_{dz} decreases by 12.9% and 74.41%. In Z4, for cases with suction effects, F_{dz} continues to decrease, as particles are lifted by the upwelling, resulting in a positive F_{dz}. In Z5, F_{dz} decreases with the increase in Z, and cases with suction pressure lead to a slightly lower F_{dz} than those without suction pressure. In summary, increasing P_{out} reduces the F_{dx} and F_{dz} experienced by particles in the jet impingement zone, causing unfavorable conditions for particles to detach from the seabed. In Fig. 12 and 13, it can be observed that increasing suction pressure weakens the impact of the front and rear jets on the seabed. Through the analysis of particle drag forces, we provide further evidence to support this observation.

The distributions of the particle velocities during the collection process at three suction pressures P_{out} are depicted in Fig. 16(d). The particle velocity V initially increases and then decreases in Z1. In Z4, particles are influenced by the upwelling, resulting in an increasing trend in V. In Z5, particles begin to move toward the nodule outlet. With every increment of 1000 Pa in P_{out}, the average V in Z5 increases by 20.69% and 11.81%, which facilitates particle transport. The variation of the particle velocities V_z in the z-direction and the particle slip velocities V_s with height Z were analyzed. In Fig. 16(e), V_z exhibits fluctuations in Z1, while in Z4, V_z consistently shows an upward trend. As the particles enter Z5, V_z gradually stabilizes. Increasing P_{out} leads to an increase in V_z in all zones. As shown in Fig. 16(f), V_s is relatively larger in Z1, and the maximum V_s decreases with the increase of P_{out}. In Z4, under conditions with suction effects, V_s exhibits a decreasing trend. In Z5, V_s gradually decreases with the increasing Z. In summary, an increase in P_{out} proves advantageous for particle transport, reducing the time nodules spend inside the collecting device and facilitating their efficient transport.

4.3 Influence of Nozzle Heights *h*/*d*

The analysis of the relationship between the drag force in the z-direction F_{dz} and the nozzle heights h/d is illustrated in Fig. 17. Average F_{dz} values are calculated in the front jet impingement zone (Z1), upwelling zone (Z4) and transport zone (Z5), resulting in curves illustrating how F_{dz} varies with h/d within these zones. In Fig. 17(a), corresponding to operating conditions with a front jet velocity V_f = 4 m/s and suction pressure P_{out} = 0 Pa, the graph clearly illustrates an increasing trend of F_{dz} in Z1 with the rising h/d, gradually approaching zero. This observation suggests a diminishing impact force on particles in Z1 as h/d increases. The F_{dz} in Z4 decreases with an increase in h/d, while F_{dz} shows no significant variation with the h/d in Z5. This implies a weakening uplifting effect on particles as h/d increases. Yet, when particles enter the collecting device and initiate transportation, the parameter h/d indicates no notable influence on particle transport. Figure 17(b) represents conditions with V_f = 4 m/s and P_{out} = –2000 Pa. The graph shows that the F_{dz} in Z1 increases with an increase in h/d. In comparison to Fig. 17(a), the rate of increase slows down, but F_{dz} ultimately decreases. This suggests that increasing suction pressure weakens the F_{dz} in Z1, affecting particle mobilization. The F_{dz} in Z4 and Z5

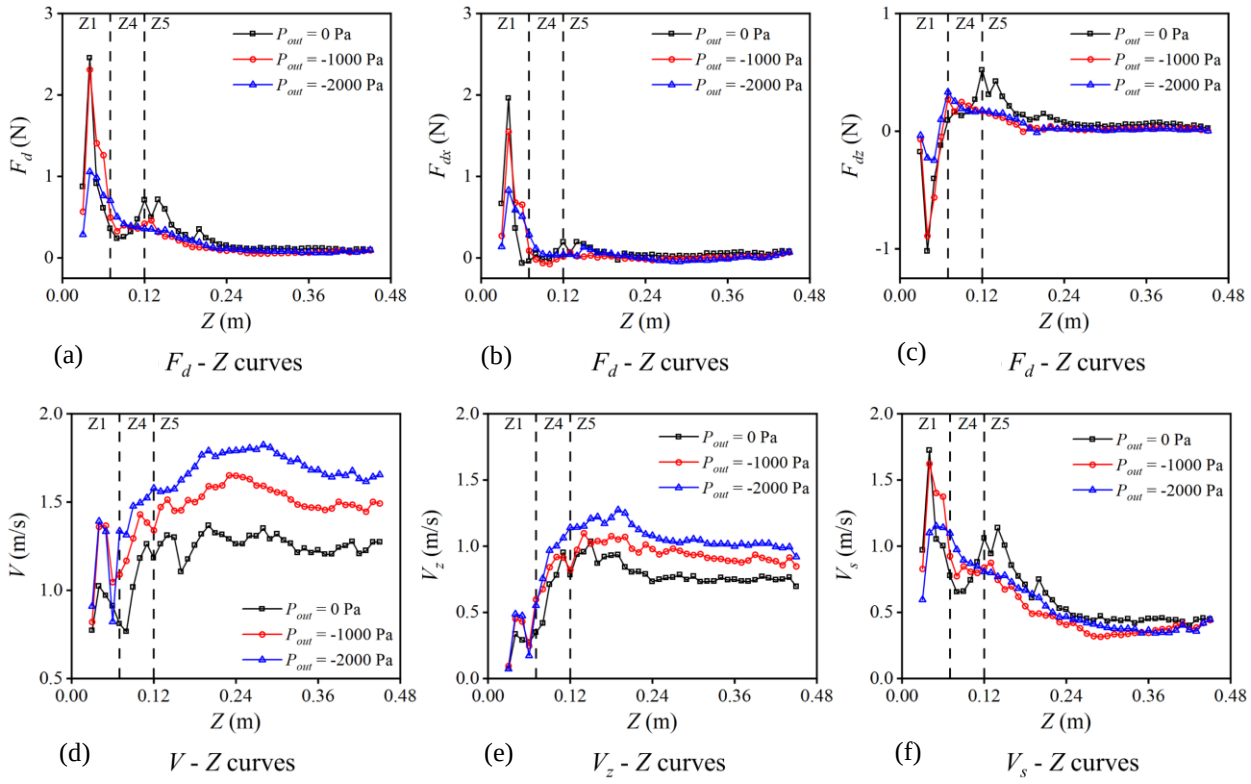

Fig. 16 Particle drag force and velocity distribution with three different P_{out} (V_f = 4 m/s, h/d = 1.05)

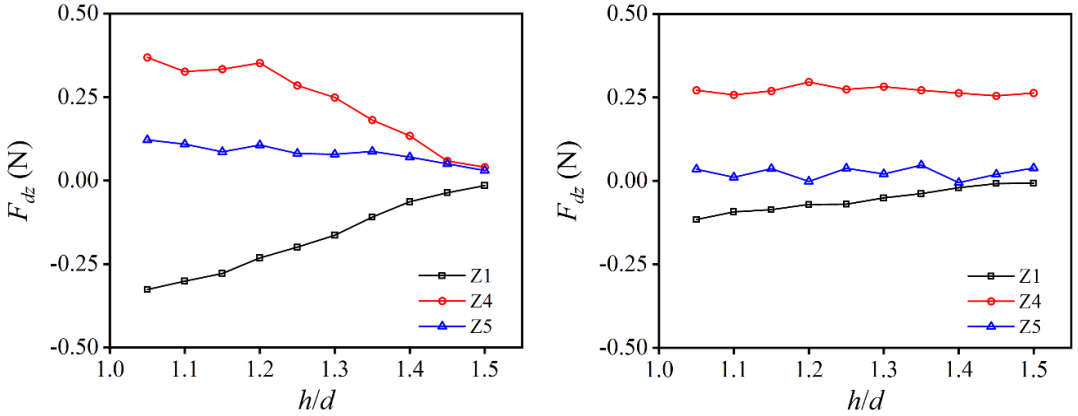

Fig. 17 Correspondence between F_{dz} and h/d

exhibits minor fluctuations with an increase in h/d but remains relatively stable overall. This observation indicates that conditions with suction pressure ensure the stability of particle lifting and transportation.

Figure 18 shows the relationship between the pick-up efficiency η and nozzle heights h/d at various front jet velocities V_f. The trends in the pick-up efficiency curves are largely similar for the three V_f in Fig. 18(a). When $h/d \leq 1.3$, variations in the collection rate are relatively minimal, with all V_f ensuring collection rates of over 80%. Nevertheless, when $h/d = 1.35$, η experiences a significant decline, with reductions of 32.14%, 46.86%, and 49.58% compared to $h/d = 1.3$ for the three V_f. When $h/d \geq 1.35$, η drops below 20%, indicating that under these conditions, the collecting device cannot meet the collection requirements. In Fig. 18(b), the relationship between the pick-up efficiency η and h/d is illustrated for three suction pressures P_{out}. It is evident that when $h/d \leq 1.3$, η exhibits fluctuations and decreases with the increasing h/d. When $h/d = 1.3$, under conditions with suction effects, η is already below 80%, and it decreases further with the increasing h/d. As $h/d = 1.35$, the reduction in η is considerably smaller for conditions with suction effects than for those without suction effects, with respective reductions of 46.86%, 31.95%, and 10.75% compared to $h/d = 1.3$ for three P_{out}. When $h/d > 1.35$, η drops below 20% for conditions without suction effects, whereas the decreasing trend in η slows down for conditions with suction effects, with η still maintained at over 40%. We believe that increasing the suction effect can enable the collection of particles even in extreme working conditions, such as $h/d > 1.3$, without the need for additional suction effects when $h/d < 1.3$, thereby reducing energy consumption.

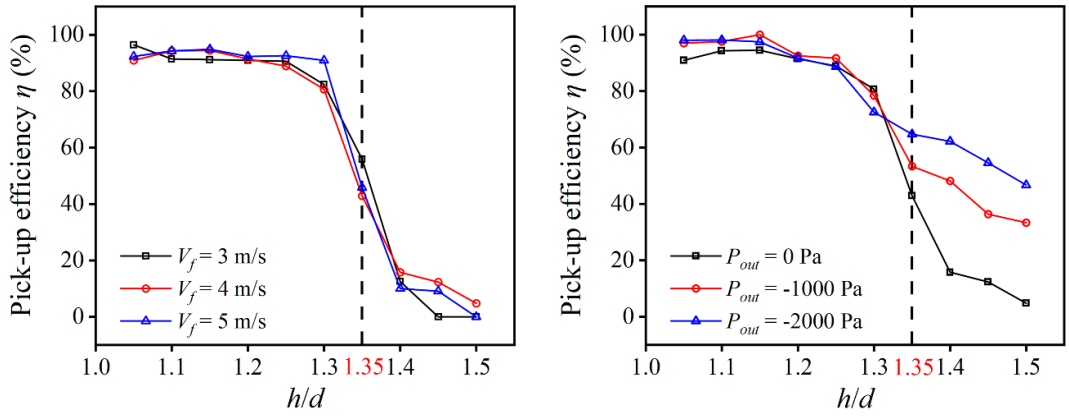

(a) η-h/d curves with different V_f (P_{out} = 0 Pa) (b)η-h/d curves with three P_{out} (V_f = 4 m/s)

Fig. 18 Correspondence between η and h/d

5. CONCLUSIONS

This study improves upon an original dual-jet collecting device. The characteristics of the flow field and particle motion at various front jet velocities V_f and suction pressures P_{out} are numerically studied. The impact of the nozzle heights h/d on the z-direction force F_{dz} and pick-up efficiency η is also explored. The main conclusions obtained are as follows:

1. An elevation in the front jet velocity V_f leads to a corresponding increase in the flow field velocity within the jet impingement zone and upwelling zone. This, in turn, leads to an increase in the drag force and particle velocity within the same zones. The pressure gradient in the confluence zone experiences an increase with the augmentation of V_f. Therefore, the lifting and transport of nodules are facilitated by the increasing V_f. The increase in V_f does not significantly affect the flow field structure. While a higher V_f facilitates particle collection, it should not be increased limitlessly. Opting for the smallest V_f possible while meeting the pick-up efficiency is advisable to conserve energy.

2. Increasing the suction pressure P_{out} results in varying degrees of lifting for the front and rear jets, making it challenging for these jets to reach the seafloor. This causes a reduction in the flow field velocity in the jet impingement zone, leading to a corresponding decrease in the particle drag force and velocity within this zone. Furthermore, the pressure gradient in the convergence zone diminishes, increasing the difficulty for particles to lift. In the upwelling zone, the flow field velocity increases under the influence of the suction pressure, consequently increasing the particle drag force and velocity and thereby facilitating particle transport. This intriguing discovery serves as inspiration for our subsequent research. When suction pressure is added, the front and rear jets intended to affect the seafloor will inevitably require increased jet velocities. The focus of our future research will revolve around controlling the relationship between suction pressure and jet velocities.

3. In the absence of suction pressures, the drag forces in the z-direction F_{dz} in both the jet impingement and upwelling zones weaken with the increasing h/d. This indicates that as h/d increases, the force exerted by the jet on the bottom diminishes, resulting in a weaker particle transport effect. When suction pressures are added, significant changes in the F_{dz} indicate that the lifting of the front and rear jets due to suction pressures leads to a substantial reduction in the F_{dz} in the jet impingement zone compared to conditions without suction pressures. This proves that the force exerted on particles during lifting movement is reduced. In the upwelling zone, F_{dz} remains stable with the changing h/d, indicating that suction pressures significantly enhance particle transport efficiency. Analyzing the variation in collection efficiency reveals that regardless of the suction pressure, efficiencies exceeding 80% are achieved when h/d < 1.3. This highlights the capability of our improved collecting device to effectively handle the collection of large-sized particles. In contrast to the significant drop in collection efficiency observed when h/d > 1.3 without suction pressures, conditions with suction pressures maintain a relatively high pick-up efficiency, exceeding 40%. Hence, we designate h/d = 1.3 as the critical number for our improved collecting device, employing dual-jet for particle collection when h/d < 1.3 and utilizing both dual-jet and suction pressures when h/d > 1.3.

ACKNOWLEDGEMENT

This work was supported by National Key Research and Development Program No. 2021YFC2801504.

CONFLICT OF INTEREST

The authors declare that they have no known competing financial interests or personal relationships.

AUTHORS CONTRIBUTION

Y. Z. Jin: Conceptualization, Methodology, Writing - Review & Editing, Formal analysis**. Q. K. Yao:** Software, Data Curation, Formal analysis, Writing - Original Draft, Visualization**. Z. C. Zhu:** Project administration, Funding acquisition**. X. M. Zhang:** Supervision, Writing - Review & Editing.

REFERENCES

Chen, Y., Xiong, H., Cheng, H., Yu, C., & Xie, J. (2020). Effect of particle motion on the hydraulic collection of coarse spherical particles. *Acta Mechanica Sinica*, *36*(1), 72-81. https://doi.org/10.1007/s10409-019-00922-6

Cho, S. G., Park, S., Oh, J., Min, C., Kim, H., Hong, S., Lee, T. H. (2019). Design optimization of deep-seabed pilot miner system with coupled relations between constraints. *Journal of Terramechanics*, *83*, 25-34. https://doi.org/10.1016/j.jterra.2019.01.003

Guo, X. S., Fan, N., Liu, Y. H., Liu, X. L., Wang, Z. K., Xie, X. T., & Jia, Y. G. (2023). Deep seabed mining: Frontiers in engineering geology and environment. *International Journal of Coal Science & Technology*, *10*(1), 23. https://doi.org/10.1007/s40789-023-00580-x

Hong, S., Choi, J. S., Kim, J. H., & Yang, C. K. (1999). *Experimental study on hydraulic performance of hybrid pick-up device of manganese nodule collector.* The Proceedings of the 3rd ISOPE Ocean Mining Symposium. https://onepetro.org/ISOPEOMS/proceedings-abstract/OMS99/All-OMS99/25731

Jia, H., Yang, J., Su, X., Wang, Y., & Wu, K. (2023). Flow characteristics and hydraulic lift of Coandă effect-based pick-up method for polymetallic nodule. *Coatings*, *13*(2), 271. https://doi.org/10.3390/coatings13020271

Kim, S., Cho, S. G., Lim, W., Lee, T. H., Park, S., Hong, S., Kim, H. W., Min, C. H., Choi, J. S., Ko, Y. T., Chi, S. B. (2024). Characterization of metal elements in deep-seabed polymetallic nodules: A multivariate statistical approach. *Marine Georesources & Geotechnology*, 1-20. https://doi.org/10.1080/1064119X.2024.2322024

Liu, L., Zhang, X., Tian, X., & Li, X. (2023). Numerical investigation on dynamic performance of vertical hydraulic transport in deepsea mining. *Applied Ocean Research*, *130*, 103443. https://doi.org/10.1016/j.apor.2022.103443

Liu, S., Yang, J., Lyu, H., Sun, P., & Zhang, B. (2024). Experimental and numerical investigation of the effect of deep-sea mining vehicles on the discharge plumes. *Physics of Fluids*, *36*(3). https://doi.org/10.1063/5.0199249

Shih, T. H., Liou, W. W., Shabbir, A., Yang, Z., & Zhu, J. (1995). A new k-ϵ eddy viscosity model for high reynolds number turbulent flows. *Computers & Fluids*, *24*(3), 227-238. https://doi.org/10.1016/0045-7930(94)00032-T

Su, X. H., Ren, Y. W., Zhu, Z. C., Yang, H., & Jia, H. (2023). Comparative study on collection performance of two back-end methods of double-row hydraulic sluicing structure in deep-sea mining. *Advanced Powder Technology*, *34*(12), 104268. https://doi.org/10.1016/j.apt.2023.104268

Xia, Q., Jia, H., Sun, J., Xi, X., & Cui, J. (2023). Study on flow characteristics of hydraulic suction of seabed ore particles. *Processes*, *11*(5), 1376. https://www.mdpi.com/2227-9717/11/5/1376

Yang, N., & Tang, H. (2003). *Several considerations of the design of the hydraulic pick-up device.* The Proceedings of the 5th(2003) ISOPE Ocean Mining Symposium, Tsukuba. https://onepetro.org/ISOPEOMS/proceedings-abstract/OMS03/All-OMS03/25117

Yue, Z., Zhao, G., Liu, M., & Xiao, L. (2021a). Experimental and numerical methods for obtaining flow field formed by hydraulic nodule pick-up devices. *International Journal of Offshore and Polar Engineering*, (3), 31. https://doi.org/10.17736/ijope.2021.jc827

Yue, Z., Zhao, G., Xiao, L., & Liu, M. (2021b). Comparative study on collection performance of three nodule collection methods in seawater and sediment-seawater mixture. *Applied Ocean Research*, *110*, 102606. https://doi.org/10.1016/j.apor.2021.102606

Zhang, Y., Lu, X., Zhang, X., Chen, Y., Xiong, H., & Zhang, L. (2021). Experimental investigation of critical suction velocity of coarse solid particles in hydraulic collecting. *Acta Mechanica Sinica*, *37*(4), 613-619. https://doi.org/10.1007/s10409-020-01022-6

Zhao, G., Xiao, L., Hu, J., Liu, M., & Peng, T. (2021a). Fluid flow and particle motion behaviors during seabed nodule pickup: an experimental study. *International Journal of Offshore and Polar Engineering*, (2), 31. https://doi.org/10.17736/ijope.2021.jc803

Zhao, G., Xiao, L., Peng, T., & Zhang, M. (2018). Experimental research on hydraulic collecting spherical particles in deep sea mining. *Energies*, *11*(8), 1938. https://doi.org/10.3390/en11081938

Zhao, G., Xiao, L., Yue, Z., Liu, M., Peng, T., & Zhao, W. (2021b). Performance characteristics of nodule pick-up device based on spiral flow principle for deep-sea hydraulic collection. *Ocean Engineering*, *226*, 108818. https://doi.org/10.1016/j.oceaneng.2021.108818